Research Article | Vol. 26, No. 12 | 11 Jun 2018 | OPTICS EXPRESS 15490
Optics EXPRESS

Manipulation of extinction features in frequency combs through the usage of graphene

Mariana Barturen,[1,2,3,5] Nicolás Abadía,[4,6] Julián Milano,[1,2] Pablo A. Costanzo Caso,[1,2] and David V. Plant[4]

[1] *Instituto Balseiro (CNEA-UNCuyo), Av. Bustillo 9500, (R8402AGP) San Carlos de Bariloche, Río Negro, Argentina*
[2] *CONICET CCT Patagonia Norte, Av. de Los Pioneros 2350, (R8402AGP) San Carlos de Bariloche, Río Negro, Argentina*
[3] *Instituto de Tecnología, Universidad Argentina de la Empresa, Lima 775, (C1073AAO) Ciudad Autónoma de Buenos Aires, Argentina*
[4] *Department of Electrical and Computer Engineering, McGill University, Montreal, QC, H3A 2A7, Canada*
[5] *mbarturen@uade.edu.ar*
[6] *nicolas.abadiacalvo@mcgill.ca*

Abstract: Lately, the integration of two-dimensional materials into semiconductor devices has allowed the modification of their effective index by simply applying a modest voltage (between 0 and 3 volts). In this work, we present a device composed of two evanescently coupled silicon microring resonators where both rings have a graphene layer on top. This design is aimed to produce frequency combs with transmission characteristics controlled upon voltage application to the graphene layer. We numerically analyze the device response as a function of the incident wavelength and applied voltage. The results showed a low input intensity (0.6 GW/cm^2) needed and a rapid response time (0.1 μs), in comparison to devices controlled by heat injection.

OCIS codes: (130.0130) Integrated optics; (230.0230) Optical devices. (190.0190) Nonlinear optics.

References and links

1. Z. Sun, A. Martinez, and F. Wang, "Optical modulators with 2D layered materials," Nat. Photonics **10**, 227–238 (2016).
2. T. Low, A. Chaves, J. D. Caldwell, A. Kumar, N. X. Fang, P. Avouris, T. F. Heinz, F. Guinea, L. Martin-Moreno, and F. Koppens, "Polaritons in layered two-dimensional materials," Nat. Mater. **16**, 182 (2017).
3. K. S. Novoselov, A. K. Geim, S. V. Morozov, D. Jiang, Y. Zhang, S. V. Dubonos, I. V. Grigorieva, and A. A. Firsov, "Electric field effect in atomically thin carbon films," Science **306**, 666–669 (2004).
4. A. K. Geim and K. S. Novoselov, "The rise of graphene," Nat Mater **6**, 183 (2007).
5. F. Schwierz, "Graphene transistors," Nat. Nanotechnol. **5**, 487–496 (2010).
6. F. Bonaccorso, Z. Sun, T. Hasan, and A. Ferrari, "Graphene photonics and optoelectronics," Nat. Photonics **4**, 611–622 (2010).
7. L. Liao, Y.-C. Lin, M. Bao, R. Cheng, J. Bai, Y. Liu, Y. Qu, K. L. Wang, Y. Huang, and X. Duan, "High-speed graphene transistors with a self-aligned nanowire gate," Nature **467**, 305–308 (2010).
8. P. Avouris, Z. Chen, and V. Perebeinos, "Carbon-based electronics," Nat. Nanotechnol. **2**, 605–615 (2007).
9. Y. Fan, N.-H. Shen, T. Koschny, and C. M. Soukoulis, "Tunable terahertz meta-surface with graphene cut-wires," ACS Photonics **2**, 151–156 (2015).
10. T. Low and P. Avouris, "Graphene plasmonics for terahertz to mid-infrared applications," ACS Nano **8**, 1086–1101 (2014).
11. Y. Fan, F. Zhang, Q. Zhao, Z. Wei, and H. Li, "Tunable terahertz coherent perfect absorption in a monolayer graphene," Opt. Lett. **39**, 6269–6272 (2014).
12. Y. Fan, N.-H. Shen, F. Zhang, Z. Wei, H. Li, Q. Zhao, Q. Fu, P. Zhang, T. Koschny, and C. M. Soukoulis, "Electrically tunable Goos–Hänchen effect with graphene in the terahertz regime," Adv. Opt. Mater. **4**, 1824–1828 (2016).
13. R. R. Nair, P. Blake, A. N. Grigorenko, K. S. Novoselov, T. J. Booth, T. Stauber, N. M. Peres, and A. K. Geim, "Fine structure constant defines visual transparency of graphene," Science **320**, 1308 (2008).
14. K. F. Mak, M. Y. Sfeir, Y. Wu, C. H. Lui, J. A. Misewich, and T. F. Heinz, "Measurement of the optical conductivity of graphene," Phys. Rev. Lett. **101**, 196405 (2008).
15. V. Sorianello, G. De Angelis, T. Cassese, M. Midrio, M. Romagnoli, M. Mohsin, M. Otto, D. Neumaier, I. Asselberghs, J. Van Campenhout, and C. Huyghebaert, "Complex effective index in graphene-silicon waveguides," Opt. Express

#322741 https://doi.org/10.1364/OE.26.015490
Journal © 2018 Received 21 Feb 2018; revised 17 Apr 2018; accepted 17 Apr 2018; published 6 Jun 2018

Optics EXPRESS

24, 29984–29993 (2016).
16. J. Capmany, D. Domenech, and P. Muñoz, "Silicon graphene waveguide tunable broadband microwave photonics phase shifter," Opt. Express **22**, 8094–8100 (2014).
17. J. Capmany, D. Domenech, and P. Muñoz, "Silicon graphene Bragg gratings," Opt. Express **22**, 5283–5290 (2014).
18. S. A. Diddams, T. Udem, J. Bergquist, E. Curtis, R. Drullinger, L. Hollberg, W. M. Itano, W. Lee, C. Oates, K. Vogel, and D. J. Wineland, "An optical clock based on a single trapped 199hg+ ion," Science **293**, 825–828 (2001).
19. M. Murphy, T. Udem, R. Holzwarth, A. Sizmann, L. Pasquini, C. Araujo-Hauck, H. Dekker, S. D'Odorico, M. Fischer, T. Hänsch, and A. Manescau, "High-precision wavelength calibration of astronomical spectrographs with laser frequency combs," Mon. Not. R. Astron. Soc. **380**, 839–847 (2007).
20. T. Steinmetz, T. Wilken, C. Araujo-Hauck, R. Holzwarth, T. W. Hänsch, L. Pasquini, A. Manescau, S. D'Odorico, M. T. Murphy, T. Kentischer, W. Schmidt, and T. Udem, "Laser frequency combs for astronomical observations," Science **321**, 1335–1337 (2008).
21. C.-H. Li, A. J. Benedick, P. Fendel, A. G. Glenday, F. X. Kärtner, D. F. Phillips, D. Sasselov, A. Szentgyorgyi, and R. L. Walsworth, "A laser frequency comb that enables radial velocity measurements with a precision of 1 cm s-1," Nature **452**, 610–612 (2008).
22. S. A. Diddams, L. Hollberg, and V. Mbele, "Molecular fingerprinting with the resolved modes of a femtosecond laser frequency comb," Nature **445**, 627–630 (2007).
23. C. Gohle, T. Udem, M. Herrmann, J. Rauschenberger, R. Holzwarth, H. A. Schuessler, F. Krausz, and T. W. Hänsch, "A frequency comb in the extreme ultraviolet," Nature **436**, 234–237 (2005).
24. R. J. Jones, K. D. Moll, M. J. Thorpe, and J. Ye, "Phase-coherent frequency combs in the vacuum ultraviolet via high-harmonic generation inside a femtosecond enhancement cavity," Phys. Rev. Lett. **94**, 193201 (2005).
25. F. Keilmann, C. Gohle, and R. Holzwarth, "Time-domain mid-infrared frequency-comb spectrometer," Opt. Lett. **29**, 1542–1544 (2004).
26. I. Coddington, W. C. Swann, L. Nenadovic, and N. R. Newbury, "Rapid and precise absolute distance measurements at long range," Nat. Photonics **3**, 351–356 (2009).
27. R. W. Boyd, *Nonlinear optics* (Academic Press, 2003).
28. G. P. Agrawal, *Nonlinear fiber optics* (Academic Press, 2007).
29. T. J. Kippenberg, R. Holzwarth, and S. Diddams, "Microresonator-based optical frequency combs," Science **332**, 555–559 (2011).
30. T. Herr, K. Hartinger, J. Riemensberger, C. Wang, E. Gavartin, R. Holzwarth, M. Gorodetsky, and T. Kippenberg, "Universal formation dynamics and noise of kerr-frequency combs in microresonators," Nat. Photonics **6**, 480–487 (2012).
31. A. A. Savchenkov, A. B. Matsko, V. S. Ilchenko, I. Solomatine, D. Seidel, and L. Maleki, "Tunable optical frequency comb with a crystalline whispering gallery mode resonator," Phys. Rev. Lett. **101**, 093902 (2008).
32. I. S. Grudinin, N. Yu, and L. Maleki, "Generation of optical frequency combs with a caf 2 resonator," Opt. Lett. **34**, 878–880 (2009).
33. W. Liang, A. Savchenkov, A. Matsko, V. Ilchenko, D. Seidel, and L. Maleki, "Generation of near-infrared frequency combs from a MgF_2 whispering gallery mode resonator," Opt. Lett. **36**, 2290–2292 (2011).
34. C. Wang, T. Herr, P. Del'Haye, A. Schliesser, R. Holzwarth, T. W. Haensch, N. Picqué, and T. Kippenberg, "Mid-infrared frequency combs based on microresonators," in Proceedings of Optical Society of America Conference CLEO: Science and Innovations (Optical Society of America, 2011), p. PDPA4.
35. I. H. Agha, Y. Okawachi, M. A. Foster, J. E. Sharping, and A. L. Gaeta, "Four-wave-mixing parametric oscillations in dispersion-compensated high-q silica microspheres," Phys. Rev. A **76**, 043837 (2007).
36. L. Razzari, D. Duchesne, M. Ferrera, R. Morandotti, S. Chu, B. Little, and D. Moss, "Cmos-compatible integrated optical hyper-parametric oscillator," Nat. Photonics **4**, 41–45 (2010).
37. J. S. Levy, A. Gondarenko, M. A. Foster, A. C. Turner-Foster, A. L. Gaeta, and M. Lipson, "Cmos-compatible multiple-wavelength oscillator for on-chip optical interconnects," Nat. Photonics **4**, 37–40 (2010).
38. M. A. Foster, J. S. Levy, O. Kuzucu, K. Saha, M. Lipson, and A. L. Gaeta, "Silicon-based monolithic optical frequency comb source," Opt. Express **19**, 14233–14239 (2011).
39. D. Braje, L. Hollberg, and S. Diddams, "Brillouin-enhanced hyperparametric generation of an optical frequency comb in a monolithic highly nonlinear fiber cavity pumped by a cw laser," Phys. Rev. Lett **102**, 193902 (2009).
40. Y. Yi, P. Pignalosa, and D. Wu, "Tunable and ultra-small graphene integrated silicon racetrack micro resonator," IEEE IEEE J. Sel. Top. Quantum Electron. **23**, 1–6 (2017).
41. P. A. Costanzo-Caso, Y. Jin, S. Granieri, and A. Siahmakoun, "Optical bistability in a nonlinear soa-based fiber ring resonator," J. Nonlinear Opt. Phys. Mater.**20**, 281–292 (2011).
42. S. Rabal, L. A. Bulus Rossini, and P. A. Costanzo Caso, "Control strategy of true time delay lines," Fiber Integrated Opt. **38**, 38–58 (2016).
43. P. Del ' Haye, T. Herr, E. Gavartin, M. Gorodetsky, R. Holzwarth, and T. J. Kippenberg, "Octave spanning tunable frequency comb from a microresonator," Phys. Rev. Lett. **107**, 063901 (2011).
44. H. Jung, C. Xiong, K. Y. Fong, X. Zhang, and H. X. Tang, "Optical frequency comb generation from aluminum nitride microring resonator," Opt. Lett. **38**, 2810–2813 (2013).
45. X. Xue, Y. Xuan, P.-H. Wang, J. Wang, D. E. Leaird, M. Qi, and A. M. Weiner, "Tunable frequency comb generation from a microring with a thermal heater," in Proceedings of Optical Society of America Conference CLEO: Science

Optics EXPRESS

and Innovations (Optical Society of America, 2014), pp. SF1I–8.
46. D. D. Smith, N. N. Lepeshkin, A. Schweinsberg, G. Gehring, R. Boyd, Q.-H. Park, H. Chang, and D. Jackson, "Coupled-resonator-induced transparency in a fiber system," Opt. Commun. **264**, 163–168 (2006).
47. C. Bao, L. Zhang, A. Matsko, Y. Yan, Z. Zhao, G. Xie, A. M. Agarwal, L. C. Kimerling, J. Michel, L. Maleki, and A. E. Willner, "Nonlinear conversion efficiency in Kerr frequency comb generation," Opt. Lett. **39**, 6126–6129 (2014).
48. S. A. Miller, Y. Okawachi, S. Ramelow, K. Luke, A. Dutt, A. Farsi, A. L. Gaeta, and M. Lipson, "Tunable frequency combs based on dual microring resonators," Opt. Express **23**, 21527–21540 (2015).
49. G. W. Hanson, "Dyadic Green' s functions and guided surface waves for a surface conductivity model of graphene," J. Appl. Phys. **103**, 064302 (2008).
50. V. P. Gusynin, S. G. Sharapov, and J. P. Carbotte, "Magneto-optical conductivity in graphene," J. Phys. Condens. Matter **19**, 026222 (2007).
51. L. Yang, T. Hu, A. Shen, C. Pei, Y. Li, T. Dai, H. Yu, Y. Li, X. Jiang, and J. Yang, "Proposal for a 2×2 optical switch based on graphene-silicon-waveguide microring," IEEE Photonics Technol. Lett. **26**, 235–238 (2014).
52. V. P. Gusynin, S. G. Sharapov, and J. P. Carbotte, "Sum rules for the optical and hall conductivity in graphene," Phys. Rev. B **75**, 165407 (2007).
53. C. Xu, Y. Jin, L. Yang, J. Yang, and X. Jiang, "Characteristics of electro-refractive modulating based on graphene-oxide-silicon waveguide," Opt. Express **20**, 22398–22405 (2012).
54. M. Liu, X. Yin, E. Ulin-Avila, B. Geng, T. Zentgraf, L. Ju, F. Wang, and X. Zhang, "A graphene-based broadband optical modulator," Nature **474**, 64–67 (2011).
55. N. M. Abadía Calvo, "Nonlinear effects in silicon ring resonators," Ph.D. thesis, Vrije Universiteit Brussels (2011).
56. Q. Lin, O. J. Painter, and G. P. Agrawal, "Nonlinear optical phenomena in silicon waveguides: modeling and applications," Opt. Express **15**, 16604–16644 (2007).
57. S. Lefrançois, "High energy pulse propagation and parametric conversion in normal-dispersion optical fibers," Ph.D. thesis, Cornell University (2012).
58. K. Liu, J. F. Zhang, W. Xu, Z. H. Zhu, C. C. Guo, X. J. Li, and S. Q. Qin, "Ultra-fast pulse propagation in nonlinear graphene/silicon ridge waveguide," Sci. Rep. **5**, 16734 (2015).
59. G. T. Reed, *Silicon photonics: the state of the art* (John Wiley & Sons, 2008).
60. Y. K. Chembo and N. Yu, "Modal expansion approach to optical-frequency-comb generation with monolithic whispering-gallery-mode resonators," Phys. Rev. A **82**, 033801 (2010).
61. Y. Okawachi, M. R. Lamont, K. Luke, D. O. Carvalho, M. Yu, M. Lipson, and A. L. Gaeta, "Bandwidth shaping of microresonator-based frequency combs via dispersion engineering," Opt. Lett. **39**, 3535–3538 (2014).
62. A. C. Turner, C. Manolatou, B. S. Schmidt, M. Lipson, M. A. Foster, J. E. Sharping, and A. L. Gaeta, "Tailored anomalous group-velocity dispersion in silicon channel waveguides," Opt. Express **14**, 4357–4362 (2006).
63. H. Haus, W. Huang, S. Kawakami, and N. Whitaker, "Coupled-mode theory of optical waveguides," J. Lightwave Technol. **5**, 16–23 (1987).
64. B. E. Little, S. T. Chu, H. A. Haus, J. Foresi, and J.-P. Laine, "Microring resonator channel dropping filters," J. Lightwave Technol. **15**, 998–1005 (1997).
65. T. Hansson, D. Modotto, and S. Wabnitz, "On the numerical simulation of kerr frequency combs using coupled mode equations," Opt. Commun. **312**, 134–136 (2014).
66. F. Gan, T. Barwicz, M. Popovic, M. Dahlem, C. Holzwarth, P. Rakich, H. Smith, E. Ippen, and F. Kartner, "Maximizing the thermo-optic tuning range of silicon photonic structures," in Proceedings of IEEE Conference Photonics in Switching, 2007, (IEEE, 2007), pp. 67–68.
67. S. Arafin, A. Simsek, S.-K. Kim, W. Liang, D. Eliyahu, G. Morrison, M. Mashanovitch, A. Matsko, L. Johansson, L. Maleki, M. Rodwell, and L. Coldren, "Power-efficient kerr frequency comb based tunable optical source," IEEE Photonics J. **9**, 1–14 (2017).
68. G. Fisichella, E. Schilirò, S. Di Franco, P. Fiorenza, R. Lo Nigro, F. Roccaforte, S. Ravesi, and F. Giannazzo, "Interface Electrical Properties of Al_2O_3 Thin Films on Graphene Obtained by Atomic Layer Deposition with an in Situ Seedlike Layer," ACS Appl. Mater. Inter. **9**, 7761–7771 (2017).

1. Introduction

Two-dimensional materials are well known for their electronic and mechanical properties [1, 2] leading to a vast number of applications . Among them, graphene is the most popular and studied specimen due to several features, e.g. its peculiar band structure [3–12]. The conduction and valence bands, touch at particular points named Dirac points. Around them, the density of states of carriers is low and consequently, graphene's Fermi energy can be significantly modified by applying a relatively low voltage. The possibility of tuning the Fermi level allows the variation of graphene's refractive index. Another extraordinary property is that the optical absorption of graphene does not depend on the wavelength in a wide range of photon energies, including the

Optics EXPRESS

traditional optical communications bands extending from mid to far infrared [13, 14].

By applying an oxide layer on top of a waveguide and a graphene sheet above, a MOS (metal-oxide-semiconductor) capacitor is built. In this way, the effective index of the complete waveguide can be varied by applying voltage to the graphene layer. This effect has been experimentally confirmed [15] and can be used to modify the optical properties of several applications [16, 17], among which, we can find frequency combs.

An optical frequency comb is an optical signal whose spectrum consists of equidistant spectral lines, i.e., on equally spaced optical frequency components. These objects have application in diverse fields as optical clocks [18], precision spectroscopy [19–22], ultraviolet and infrared spectroscopy [23–25], precision distance measurement [26], etc.

A usual method used to produce optical combs consists of a continuous wave laser coupled to a resonator which operates in the nonlinear regime. Usually, the resonator is fabricated with a third order nonlinear material which allows degenerated four-wave mixing (FWM). The frequency conversion mechanism that takes place inside the resonator's material, lies on the intensity dependence of the refractive index. In this process, two pump photons are annihilated and a new pair of photons is created: one of an up-shifted frequency called signal, and another of a downshifted frequency called idler. Provided the momentum and energy conservation, the new born waves are equidistant in frequency from the pump wave. When the optical cavity decay rates are surpassed by the scattering rate into the signal and idler modes, the parametric process occurs, yielding to symmetric sidebands that grow in intensity with increasing pump power and the frequency comb is produced [27–30].

If the signal and idler frequencies coincide with optical microresonator modes, the parametric process is enhanced, resulting in efficient sideband generation.

The power threshold for the initiation of parametric oscillation scales with the inverse of the quality factor Q squared. From this relation, it is possible to see the advantages of using a high quality factor. Furthermore, the required power to start the parametric oscillation can be strongly reduced [30–39]. Linear and nonlinear ring resonators were extensively analyzed in different applications [16, 40–42].

When building a device destined to produce frequency combs, many parameters are fixed after the fabrication process, among which we can find the resonance frequency and the coupling strength to the bus waveguide. In the case of having only one resonator, the only parameter that can be varied after building the device, is the resonance frequency. This is achieved by manipulating the resonator effective index, using different techniques [43–45]. In the case of two coupled resonators, when the effective index is changed, not only the the resonance frequency is modified, but also the overall structure coupling to the bus waveguide as it is explained, for instance, in reference [46]. This coupling strength syntonization allows a more precise manipulation of the parameters that play a role in the comb building process [47].

We propose the usage of a graphene layer to change the effective index of two coupled microrring resonators in order to control the properties of the generated frequency comb. Our design aims for the advantages of rapid response time and low power consumption in comparison with the traditional method of heat transfer [48].

In the first part of this work, we analyze the effective index in the SOI-graphene structure. Secondly, we verify that the FWM is present and it is significant in comparison to other non-linear processes. After that, we continue by describing the frequency comb generation device and how the manipulation of the extinction futures is achieved.

2. SOI-graphene effective index

To model graphene, we follow the approach schemed in [49]. The graphene sheet is modeled as an extremely thin layer with a conductivity $\sigma(\omega, \mu_c, \Gamma, T)$, being ω the angular frequency, μ_c the chemical potential, Γ the scattering rate (assumed to be independent of energy [49]) and T

Optics EXPRESS

the temperature. Starting from the Kubo formula [50] and considering no magnetic field, the intraband (σ_{intra}) and interband (σ_{inter}) contributions to the conductivity are identified:

$$\sigma = \sigma_{intra} + \sigma_{inter} \tag{1}$$

The intraband term results:

$$\sigma_{intra} = -i\frac{e^2 k_B T}{\pi\hbar^2(\omega - i2\Gamma)}\left(\frac{\mu_c}{k_B T} + 2ln(e^{-\mu_c/k_B T} + 1)\right) \tag{2}$$

where e is the electron charge, k_B is the Boltzmann constant and $\hbar = h/2\pi$ is the reduced Planck constant. Γ can be calculated as $\Gamma = e\,{v_F}^2/(\mu\,\mu_c)$ being v_F the Fermi velocity in graphene and μ the electron mobility. A typical value is $1/2\Gamma = 5\times10^{-13}$ s [51].

When analyzing the energies involved in the conductivity formula we find that thermal energy is two orders of magnitude lower than photon energy and chemical potential ($k_B T \ll |\mu_c|, \hbar\omega$). In this case, the interband conductivity can be approximated as [52]:

$$\sigma_{inter} \simeq \frac{-ie^2}{4\pi\hbar}\left(\frac{2|\mu_c| - (\omega - i2\Gamma)\hbar}{2|\mu_c| + (\omega - i2\Gamma)\hbar}\right) \tag{3}$$

Provided the conductivity, the dielectric constant (ϵ_g) can be calculated as:

$$\epsilon_g = 1 + \frac{i\sigma(\omega)}{\omega\epsilon_0\Delta} \tag{4}$$

where $\Delta = 0.34$ nm is the thickness of the graphene layer and ϵ_0 is the vacuum dielectric constant. A graphene monolayer is only one carbon atom in diameter. Given ϵ_g, the real (n_g) and imaginary (k_g) parts of graphene's refractive index can be determined using the relation $n_g + ik_g = \sqrt{\epsilon_g}$.

By applying a suitable voltage V_g between the graphene layer and the Si core, the chemical potential μ_c can be modified and, as a consequence, the refractive index is also varied [53]:

$$|\mu_c(V_g)| = \hbar v_F\sqrt{\pi|\eta(V_g - V_0)|} \tag{5}$$

where $V_0 = 0.8$ V is the offset from zero caused by natural doping and $\eta = 9\times10^{16}$ 1/(Vm^2) [54]. Fig. 2(a) exhibits n_g and k_g calculations as a function of V_g and μ_c. It can be observed that with a modest excursion of 1 V, n_g can be varied in an order of 3.

This variation of refractive index can be profited to modify the effective index in a semiconductor waveguide. To explore this effect, we have performed finite-element simulations using an ad-hoc software that solves the Helmholtz Eq. and including the electrical conductivity of graphene as a function of the chemical potential, i.e. the applied voltage, and the incident wavelength. The incident wavelength was 1550 nm for the complete set of calculations. Fig. 1 shows the simulation geometry. The dimensions of the waveguide were chosen in order to obtain sufficient evanescent wave so the coupling between adjacent waveguides was possible. The silicon (Si) core was 200 nm width and 500 nm high and it was surrounded by silica. The green layer in Fig. 1 represents a doped Si region used to apply the voltage between the Si-core and the graphene layer. With this transversal area the waveguide results monomode. On top of each microrring resonator an Al_3O_2 layer is deposited with a graphene sheet above. Finally, an air layer covered the waveguide. Scattering boundary conditions were used in the geometry limits. The employed refractive indexes were $n_{Si} = 3.47$ for silicon, n_{SiO2}=1.44 for silica and n_{Al2O3}=1.74 for Al_2O_3, for a wavelength of 1550 nm. In the case of graphene, its refractive index was included as a function of applied voltage as it was explained in the previous section. An example of the field distribution in the TM_0 is shown in Fig. 2(b). The results for the variation of the effective index in the TM_0 mode are exhibited in Fig. 2(c). It can be seen that with a small voltage variation of 1 V the effective index can be varied in 10^{-3}. These results agree with experimental data [15].

Optics EXPRESS

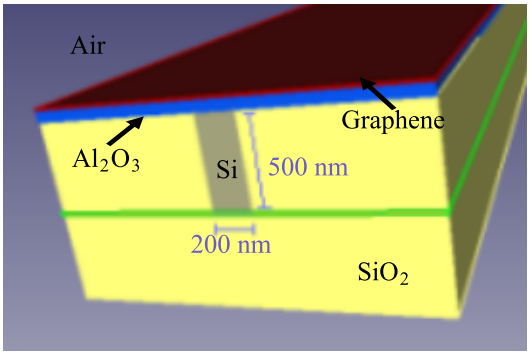

Fig. 1. Geometry utilized in the finite-elements simulations. The Si core is 200 nm with and 500 nm height. It is surrounded by SiO_2 and it has a Al_2O_3 layer on top with a graphene sheet above. The green layer represents a doped Si region of 60nm thickness, used to apply the voltage between the Si-core and the graphene layer.

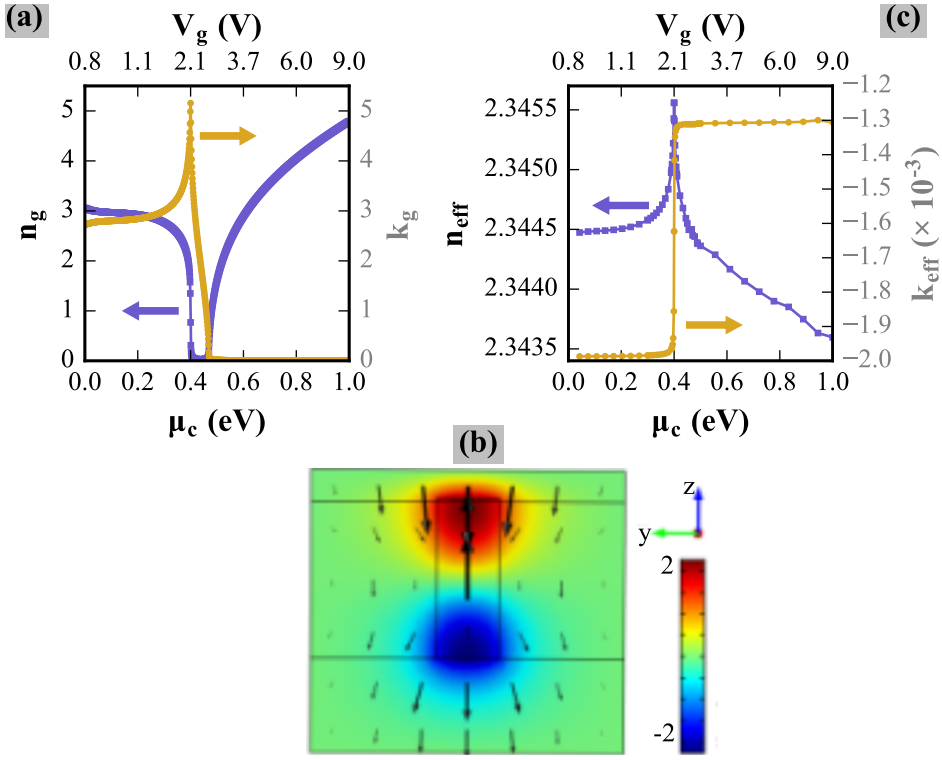

Fig. 2. **(a)** Real (n_g) and imaginary (k_g) components of graphene's refractive index, obtained from Eqs. (1), (2), (3) and (4) for $\lambda = 1550$ nm, as a function of chemical potential μ_c and applied voltage V_g . **(b)** Example of the field distribution in the TM_0 mode for a chemical potential of 0.4 eV. The background colors represent the field normal to the surface, where the color scale is in units of V/m. The arrows show the field in the surface y-z. **(c)** Real (n_{eff}) and imaginary (k_{eff}) components of the effective index of the first transversal magnetic mode TM_0 obtained by finite-elements simulations performed for the geometry shown in Fig.1.

Optics EXPRESS

3. Non-linear context

Several processes occur in the non-linear medium at the same time. To quantify them we have simulated the beam propagation through the non-linear medium using the non-linear Schrödinger Eq. for the Pump, Stokes, and anti-Stokes signals inside the SOI waveguide [55,56]. We also took into account spontaneous Raman which was modeled adding a term to the Stokes and anti-Stokes modes Eqs., that depends on the pump intensity [57]. These coupled Eqs. were solved using the split-step Fourier method [28]. Since light completes several round trips before leaving the rings it becomes necessary to calculate the effective length, L_{eff} thorough which the beam travels. Following Ref. [58], $L_{eff} = 1/(2Im(\vec{k}))$, where $\vec{k}$ is the complex propagation wavevector and $|\vec{k}| = 2\pi n_{eff}/\lambda$. For our waveguide results $L_{eff} \simeq$1mm. For these simulations, there was no Stokes signal stimulated.

On the other hand, the simulations show, as it is expected in Si, losses are very high due to free carriers generated by two photon absorption. We neglect these losses since they can be avoided by removing carriers with a p-n junction in reverse bias as it is the common procedure [59]. The total linear loss calculated was 0.13 GW/cm^2.

Regarding the comb stability, in [60,61] it is explained why the case of anomalous dispersion is much more suitable than normal dispersion. The FWM process is highly affected by the effects of self-phase and cross-phase modulation (SPM and XPM). These processes refer to the nonlinear phase modulation of a beam, caused by its own intensity (SPM) or by other modes intensity (XPM), via the Kerr effect. In order to overcome these phenomena, the waveguide anomalous dispersion can be used. We performed a last set of finite-element simulations to verify that this effect is possible in our waveguides. In this case, we used the geometry of Fig. 1 and implemented the Sellmeier Eqs. to provide the model with an input for the dispersion of Si and SiO_2 [62]. Once the effective index was obtained as a function of the incident wave frequency, the group velocity dispersion (GVD) was calculated through [27],

$$GVD(\omega_0) = \frac{2}{c}\left(\frac{\partial n}{\partial \omega}\right)_{\omega=\omega_0} + \frac{\omega_0}{c}\left(\frac{\partial^2 n}{\partial \omega^2}\right)_{\omega=\omega_0} \tag{6}$$

After the GVD is extracted, the dispersion parameter D can be derived through $D = -2\pi c/(\lambda^2).GVD$. The results are shown in Fig. 3 for a particular chemical potential of $\mu_c = 0.8$ eV. It can be seen that anomalous dispersion ($D > 0$) is achieved for a certain range of wavelengths including $\lambda \simeq 1550$ nm, which is our selected wavelength.

In recent publication [58], the effective waveguide kerr coefficient n_{2eff} is calculated which results at least three times major than that of silicon. We have followed their procedure to calculate this coefficient for our waveguide, finding $n_{2eff} = 9.75 \times 10^{-17}$ m^2/W, which is one order of magnitude higher than that of silicon.

To evaluate these nonlinear effects we have calculated characteristic lengths of each process. For SPM we have $L_{SPM} = 1/(\gamma P_{norm})$, where $\gamma = n_{2eff}\omega/c$ and P_{norm} is the incident power normalized by the waveguide area. In our case, the selected value of P_{norm} is justified with in the comb formation theory and will be explained later. We used the value $P_{norm} = 1.74x103$ W/cm^2. The dispersion length has been calculated as $L_D = \tau^2 2\pi c/(D\lambda^2)$, where τ is typical time related to the pump. Since our model uses continuous incident wave, we have chosen $\tau = 2\pi/\omega = 5\times10^{-15}s$. The obtained values for both lengths were L_{SPM} =247 m and L_D =0.4 m, indicating that the effect of anomalous dispersion is stronger than the self-phase modulation one. The major conclusion is that both lengths result orders of magnitude larger than the waveguide effective length $L_{eff} \simeq$1 mm, meaning that there will not be a big distortion in our mode profile.

Optics EXPRESS

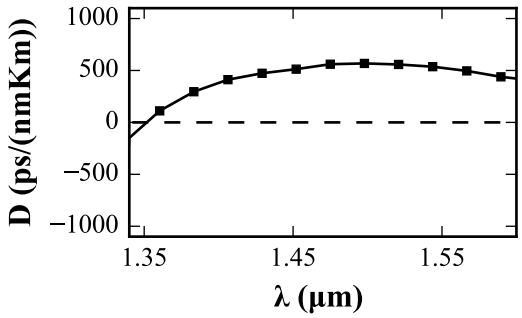

Fig. 3. Group velocity dispersion parameter D as a function of wavelength λ for a chemical potential of μ_c = 0.8 eV. The simulations were performed for the geometry of Fig 1.

4. Frequency comb generation device

The proposed analysis consists of two microrings evanescently coupled to a bus waveguide as shown in Fig. 4. Both rings possess a straight coupling section of 0.4 μm length in order to facilitate the passage of the incident wave to the rings. We worked with two options for the radio of the circular parts: 5 μm or 30 μm. These radius were chosen from a trade-off between minimizing the device size and having enough optical path to achieve an effective index change of the order of 10^{-3}, the one achievable with graphene, produces a significant phase shift. Given the high contrast between the refractive index of Si and SiO_2, we chose a 200 nm width core in order to have some evanescent field outside the core. This condition was necessary for the coupling between the microring resonators. The width of the total microring resonators, including the silica cladding, was 4 μm. Each ring has a 10 nm thick Al_2O_3 layer on top of the core with a graphene sheet above. With this thickness a MOS capacitor is formed between the graphene layer and the Si core. The resulting waveguide is monomode since the incident frequency is lower than the cutoff frequency of the first TM mode.

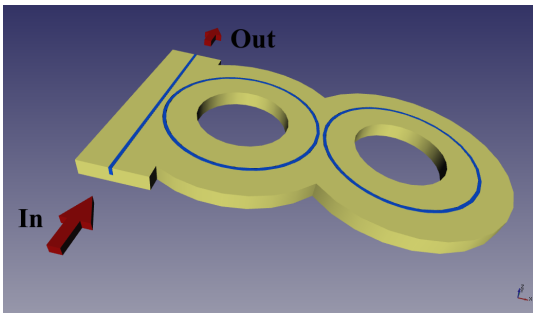

Fig. 4. Schematic of the proposed device. The geometry consists of two evanescently coupled Si microring resonators and a bus waveguide. The surrounding material is SiO_2. The Si core is 0.2 μm width and the SiO_2 cladding is 4 μm width.

Since the two cavities are evanescently coupled, the individual cavity modes hybridize and, as a result, a symmetric and an anti-symmetric supermodes exist. According to the coupled-mode

Optics EXPRESS

theory, these supermodes eigenfrequencies are given by [63]:

$$\omega_{\substack{sim \\ antisim}} = \omega_{avg} \pm \sqrt{\frac{\Delta\omega^2}{4} + K_\omega^2} \tag{7}$$

where ω_{avg} is the average resonant frequency (between the two cavities), $\Delta\omega$ is the difference between the individual cavity resonances (cavity detuning), and K_ω is the inter-ring temporal coupling rate. In the case of degenerated cavities ($\Delta\omega = 0$), the supermode resonances are separated by $2K_\omega$.

We performed 2D finite-elements simulations with the aim of investigating the response of our system and comparing it with the predictions of Eq. (7). We solved the Helmholtz Eq. in our domain of interest with an ad-hoc software using the beam envelopes approach, first order elements and scattering boundary conditions in every geometry limit. For the first set of simulations the refractive index of both rings was kept equal.

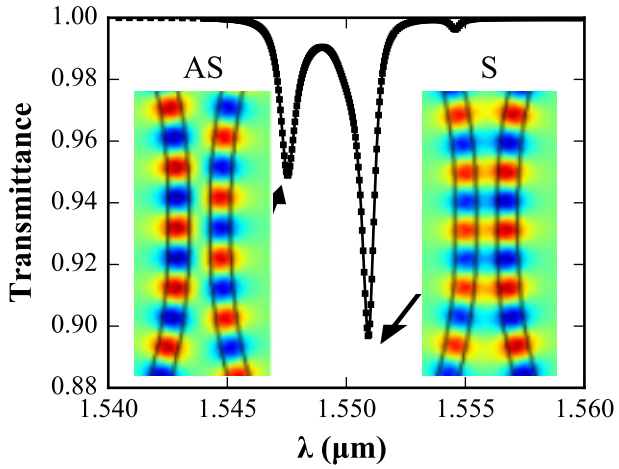

Fig. 5. Transmittance as a function of the wavelength for microring resonators of radius R = 5 μm. The two supermodes, symmetric (S) and antisymmetric (AS) can be observed. The distribution of the out-of-plane field component, E_z, is also shown to clearly visualize the modes parity.

The resulting transmittance at the end of the bus waveguide is shown in Fig. 5, as a function of the wavelength λ. The symmetric and antisymmetric modes could be identified as described by Eq. (7). The out-of-plane field in the inter-ring coupling zone is also presented to clearly visualize the parity of the supermodes. All the presented results belong to the first transversal electric mode TE_0.

In a second set of simulations we varied the relative refractive index of the core of the two rings. We define ε as the maximum change that can be produced in n_{eff} by applying voltage to the graphene layer. We have stated before its value being $\varepsilon = 10^{-3}$ which can be achieved by changing the applied voltage in 1 V. In order to modify the relative effective index we left the first ring with a fixed index of $n_1 = n_{Si} + \varepsilon/2$, and varied the index of the second ring as $n_2 = n_1 + \Delta n$ with $-\varepsilon/2 \leq \Delta n \leq \varepsilon/2$, which means to vary the applied voltage between -0.5 V and 0.5 V. In this way, positive and negative detuning between the two microring resonators was possible preserving the total excursion (1 V).

The calculated transmittance as a function of incident wave frequency is shown in Fig. 6, for

Optics EXPRESS

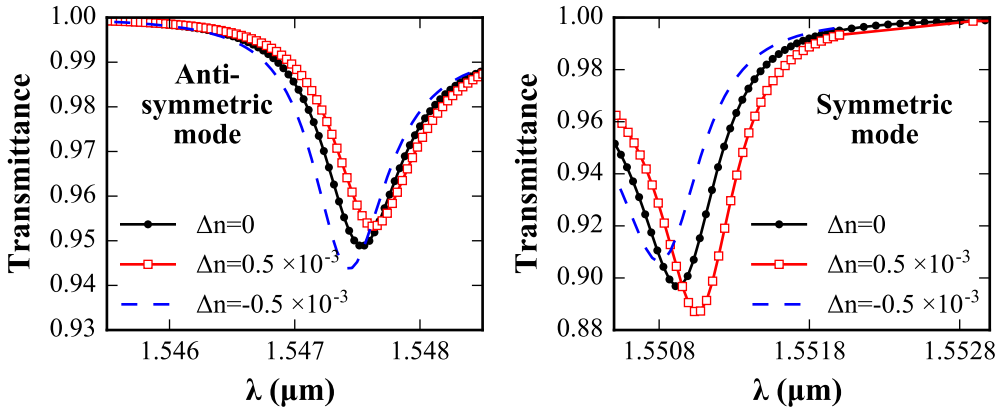

Fig. 6. Symmetric and antisymmetric modes transmittance as a function of the wavelength for different detuning values. The results correspond to rings of a radius of 5 μm.

rings of 5 μm radius, and in Fig. 7 for rings of 30 μm radius. In both cases the behavior predicted by (7) is observed. The supermodes intensity depends on K_ω [63] and, since K_ω is a function of the wavelength and refractive indexes [64], the intensity finally depends on these two parameters and also does the transmittance. K_ω also depends on the radius of the rings [64] and this is the reason why the shift achieved in the case of the smallest radius is minor than the one obtained for the 30 μm radius case.

As a result, the transmittance of the proposed device can be significantly varied by applying a modest voltage. This tunable transmittance can be profited as an envelope for the frequency comb components that allows to diminish, as well as magnify specific spectral lines.

To exemplify this point, we have performed numeric simulations. The comb lines, can be modeled by a system of coupled Eqs. [60]:

$$\begin{aligned}\frac{\partial A_\mu}{\partial t} &= -\frac{1}{2}\Delta\omega_\mu A_\mu + \delta_{\mu,0}\frac{1}{2}\Delta\omega_0 F e^{i(\omega_p-\omega_0)t} \\ &- ig_0\sum_{\alpha\beta\gamma} A_\alpha A_\beta^* A_\gamma e^{i(\omega_\alpha-\omega_\beta+\omega_\gamma-\omega_\mu)t}\end{aligned} \tag{8}$$

where intermodal coupling is assumed. The modes amplitude is normalized so $|A_\mu|^2$ is the instantaneous number of photons in the mode μ. Each mode μ has a frequency $\omega_\mu = \omega_0 + D_1\mu + 0.5D_2\mu^2$, where D_1 corresponds to the free spectral range (FSR) of the resonator and D_2 to the difference between two neighboring FSRs at the center frequency ω_0. In Eq. (8), A_μ is the amplitude of the mode μ, t is the time, $\Delta\omega_\mu$ is the modal bandwidth, F is the external pumping factor which is normalized in a way such that $|F|^2$ represents the total number of photons that are coupled into the cavity and g_0 is the FWM reference gain. ω_μ is the modal frequency and ω_p is the pump frequency. The second term in Eq. (8) describes the external pumping and it adds up only for $\mu = 0$ and the last term describes the frequency mixture that occurs in the FWM process.

We solved Eq. (8), that is stated for a single resonator, using the methodology proposed in [65] and a split-step Fourier algorithm. To model the structure, i.e. two coupled resonators, we then split each obtained mode following Eq. (7) and, after that, we multiplied the result by the coupled resonators efficiency. The calculus were carried out considering $\Delta\omega_\mu = \Delta\omega_0$ which is a fair assumption as can be observed in Fig. 7. $\Delta\omega_0$ was extracted from the finite-element simulations being $\Delta\omega_0 = 45$ GHz. The pump frequency was chosen to be $\omega_p = 1232$ rad/s and

Optics EXPRESS

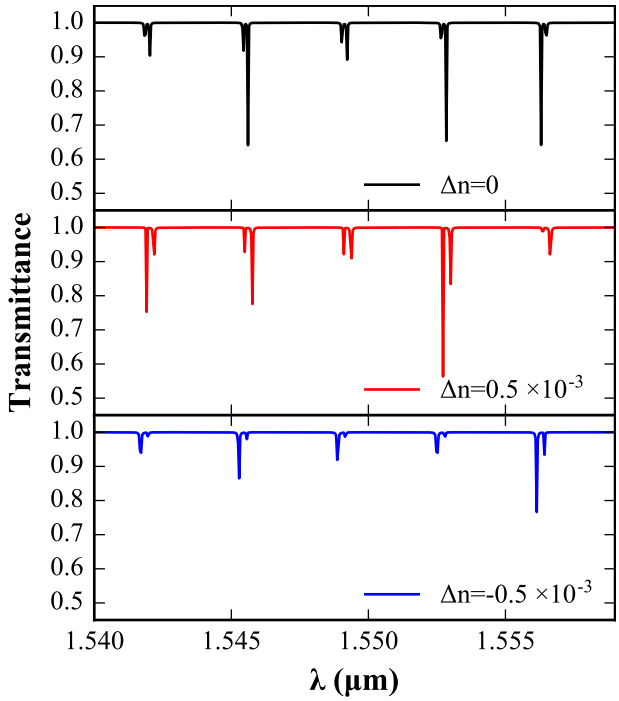

Fig. 7. Transmittance as a function of the wavelength for different detuning values. The results correspond to rings of a radius of 30 μm.

g_0 = 3MHz. As it is explained in [60] there is a power threshold for the initiation of the nonlinear effects, that can be translated into a threshold number of photons $\left|A_0^{th}\right|^2 = 0.5\Delta\omega_0/g_0$. We chose to express the parameter F in units of this quantity. Once we have the threshold number of photons we can calculate the power threshold and normalize it by the waveguide area resulting 4.31×10^{-5}GW/cm^2. For the simulations we used $F = 3|A_0|^2$. The selected total time for the simulations was 0.1 μs.

Results are shown in Fig. 8. It can be observed that the same line can be suppressed or amplified depending on the value of Δn, i.e. on the applied voltage. The insets zoom in the evolution of the central modes. We can observe that for $\Delta n = 0.5 \times 10^{-3}$ the first mode has a slower intensity than the second mode. When $\Delta n = -0.5 \times 10^{-3}$ the second mode has higher intensity than the first one. This shows that the relation between the intensities of these two modes is inverted when we change Δn, that is to say when we change the applied voltage.

After that, we will estimate the response time of the system in order to compare it to other methods. In [60], it is established that the difference between the pump frequency and the resonator's resonance frequency, σ, establishes a condition for certain modes to be excited. At power threshold, for the mode μ to be stable it is necessary that $\sigma + 0.5\bar{\omega}_\mu < -\sqrt{3}/2\Delta\omega_0$ where $\bar{\omega}_l = \omega_\alpha - \omega_\beta + \omega_\gamma - \omega_\mu$ referencing the frequencies involved in the four-wave mixing process. In our case, this stability condition is achieved for the six first modes, $\mu \in \{-6, ..., 6\}$, and this was verified in the simulations (not shown). Only the six first spectral lines were activated when the incident power was at threshold.

On the other hand, after 0.1 μs these six components had already appeared so we considered this time as representative for the response time in a single resonator. We established this time as the lower limit for the response time of the coupled resonators device. Furthermore, we need to

Optics EXPRESS

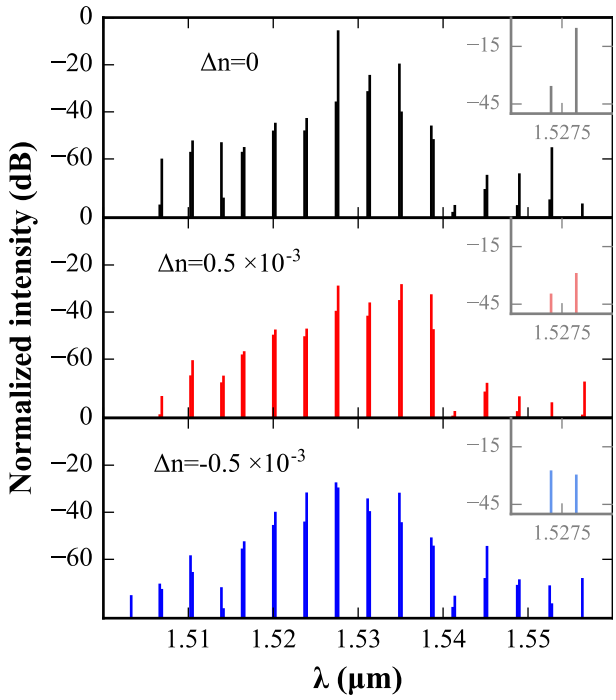

Fig. 8. Normalized intensity as a function of the wavelength for different values of Δn. The results correspond to rings of a radius of 30 μm. The insets zoom in the evolution of the central mode for the different Δn.

consider the speed at which the change in the refractive index is produced. In the literature we can find modulators made of Si and graphene that reach modulations speeds ranging from 1 to 30 GHz [1]. With this information we estimate a time response for this effect of the order of 30 ps. We notice that this time is significantly minor than the time needed to stabilize the comb. So, our final estimation of the response time is 0.1 μs. This is a remarkable advantage when we compare this device with others that employ the thermo-optic effect [48] since they have slower response time, i.e. in the order of microseconds [66] and they also need to deal with issues of thermal volumetric expansion.

A word must be said concerning SPM and XPM. The processes can introduce additional detunings $\Delta\omega_{SPM}$ and $\Delta\omega_{XPM}$ and, as a consequence, they can limit the comb span. To investigate these effects we have calculated the detunings they produce, taking into account the graphene presence by using the kerr index n_{2eff} calculated as explained in Ref. [58]. Since we are using a continuous incident wave, the SPM frequency shift coefficient can be calculated as $2\pi n_2 I_0 L_{eff}\omega_0/\lambda_0$ where I_0 is the incident intensity and all the other parameters were defined before. Evaluating this expression we obtain $\Delta\omega_{SPM} \simeq 23$ rad/s and $\Delta\omega_{XPM} \simeq 88$ rad/s. To calculate the XPM contribution we took an extreme case were the six modes present at threshold condition contribute in the same way to XPM and each mode intensity was extracted in relation to the central mode. With the obtained values the new detuning σ was calculated. Finally, the stability condition was once more verified to find that only six modes are allowed at threshold, meaning that SPM and XPM effect do not change the comb structure.

Continuing with the comparison with the method of thermal injection, we can say that voltage can be applied much more locally than heat.

Optics EXPRESS

In addition to this, since the envelope of the comb components can be manipulated in-situ, the proposed system also has the property of simplifying, to certain extent, the amendment of unavoidable imperfections in the fabrication process after the device is built.

Another important advantage of the proposed device arises when looking at the consumed power. The comb simulations results show that a power 1.3×10^{-4}GW/cm^2 destined to the FWM process is enough to produce the comb. To achieve this situation, an input intensity of 0.6 GW/cm^2 is sufficient. This is considered a low input intensity [67] and makes the device suitable for many applications.

We have also estimated the electrical power consumption. Using as starting point reference [68] we have estimated power consumption of 5 mW which results in the same order of magnitude of that needed by the electric heating method [48].

5. Conclusion

We have proposed a device for frequency comb generation that allows in-situ tunability of the comb characteristics. The geometry contains two coupled SOI microrings coupled to a bus waveguide. The inter-ring coupling can be modified through low intensity voltage applied to a graphene layer lying on top of one of the microrings. We have numerically analyzed the response of the prototype as a function of the applied voltage and incident wavelength.

In comparison to thermal heating, which is commonly used to manipulate the comb characteristics, this device has the potential of offering lower response time, low input intensity and small footprint.

In addition, the calculated power consumption resulted low which makes it suitable for many applications.

Funding

Universidad Nacional de Cuyo (C014); CONICET, Comisión Nacional de Energía Atómica (CNEA); Sofrecom Argentina; Universidad de la Empresa (Research project P17T02).

Acknowledgments

We would like to acknowledge Condensed Matter Theory Group belonging to Bariloche Atomic Center for the provision of the cluster where the calculations were performed.